IEEE Access
Multidisciplinary ⋮ Rapid Review ⋮ Open Access Journal

Received 6 March 2024, accepted 20 March 2024, date of publication 29 March 2024, date of current version 17 April 2024.

Digital Object Identifier 10.1109/ACCESS.2024.3383323

RESEARCH ARTICLE

Data-Driven Modeling of Grid-Forming Inverter Dynamics Using Power Hardware-in-the-Loop Experimentation

NISCHAL GURUWACHARYA[1,2], (Student Member, IEEE), SOHAM CHAKRABORTY[3], (Member, IEEE), GOVIND SARASWAT[4], (Senior Member, IEEE), RICHARD BRYCE[2], (Senior Member, IEEE), TIMOTHY M. HANSEN[1], (Senior Member, IEEE), AND REINALDO TONKOSKI[5], (Senior Member, IEEE)

[1]Department of Electrical Engineering and Computer Science, South Dakota State University, Brookings, SD 57007, USA
[2]National Renewable Energy Laboratory, Golden, CO 80401, USA
[3]Department of Electrical and Computer Engineering, University of Minnesota, Minnesota, MN 55455, USA
[4]Enphase Energy, Austin, TX 78758, USA
[5]Department of Electric Power Transmission and Distribution, Technical University of Munich, 80333 Munich, Germany

Corresponding author: Nischal Guruwacharya (nischal.guruwacharya@jacks.sdstate.edu)

This work was supported in part by the Advanced Research Projects Agency-Energy (ARPA-E) through the Project Rapidly Viable Sustained Grid under Grant DE-AR0001016; in part by U.S. Department of Energy Office (DOE) of Science, Office of Electricity Microgrid Research and Development Program, and Office of Energy Efficiency and Renewable Energy Solar Energy Technology Office under the EPSCoR Grant DE-SC0020281; in part by NSF under Grant OIA-2316399; and in part by the National Renewable Energy Laboratory funded by Alliance for Sustainable Energy, LLC, for DOE under Contract DE-AC36-08GO28308.

ABSTRACT Recently, there is rapid integration of power electronic converter (PECs) into the power grid. Most of these PECs are grid-following inverters, where weak grid operation becomes an issue. Research is now shifting focus to grid-forming (GFM) inverters, resembling synchronous generators. The shift towards converter-based generation necessitates accurate PEC models for assessing system dynamics that were previously ignored in conventional power systems. Data-driven modeling (DDM) techniques are becoming valuable tools for capturing the dynamic behavior of advanced control strategies for PECs. This paper proposes using power hardware-in-the-loop experiments to capture dynamic GFM data in the application of DDM techniques. Furthermore, the paper derives an analytical approach to obtaining a mathematical model of GFM inverter dynamics and compares it with the DDM. A square-chirp probing signal was employed to perturb the active and reactive power of the load inside an Opal-RT model. The dynamic response of the GFM inverter, including changes in frequency and voltage, was recorded. This data was then used in a system identification algorithm to derive the GFM DDMs. The effectiveness of DDM is cross-validated with an analytical approach through experimental simulation studies, and the goodness-of-fit for both approaches is compared. Both approaches show more than 85% accuracy in capturing the dynamic response of GFM inverters under different loading conditions.

INDEX TERMS Data-driven modeling, grid-forming inverter, power hardware-in-the-loop, power system dynamics, real-time digital simulator, system identification.

NOMENCLATURE

DDM	Data-driven modeling.
EMT	Electromagnetic transients.
GFL	Grid-following.
GFM	Grid-forming.
GoF	Goodness-of-fit.

The associate editor coordinating the review of this manuscript and approving it for publication was Meng Huang.

NRMSE	Normalized root-mean-square-error.
PCC	Point of common coupling.
PECs	Power electronic converters.
PHIL	Power-hardware-in-the-loop.
PLL	Phase-locked Loop.
PWM	Pulse-width modulation.
RTS	Real-time simulator.
SysId	System identification.
TF	Transfer function.
UDP	User datagram protocol.

I. INTRODUCTION

The increasing interest in renewable energy and batteries has made power electronic converters (PECs) a critical component of power distribution networks [1]. As converter-based generation is used to meet the future energy demand, having accurate models that represent the interaction between the grid and PECs is crucial. The response of PEC-based generation involves faster and more stochastic dynamics compared to traditional power systems due to their fast-switching mechanisms [2], [3]. In the past, these dynamics were largely neglected because the percentage of PEC-based generation was low, and the PECs had a passive role without actively contributing to power system voltage and frequency control. This neglect was possible because power system dynamics were primarily governed by large synchronous generators with well-defined models [4].

The electrical grid is undergoing a seamless transition where rotating synchronous machines are being replaced by PECs. This transition introduces a low-inertia system with a novel type of dynamic behavior [5], [6]. PECs control can be categorized into two types: grid-following (GFL) and grid-forming (GFM). GFL inverters, commonly used in grid-connected applications with current control, regulate the ac-side current by following the phase angle and frequency of the existing grid voltage using a phase-locked loop (PLL) mechanism [7], [8]. On the other hand, GFM inverters manage the ac-side voltage and play a crucial role in forming a controllable voltage source, allowing them to set the grid's reference voltage and frequency. They achieve synchronization with the rest of the grid using frequency droop control (typically $P-\omega$ droop), similar to traditional synchronous generators [9], [10], [11]. Various GFM control methods have been proposed in the literature, including droop control, virtual synchronous machines, and virtual oscillator controllers [12], [13], [14]. In the electrical grid, GFL inverters primarily function as current sources and can provide auxiliary services according to IEEE 1547, such as droop-based reactive power support [15]. They are commonly used for integrating renewable energy sources like wind and solar energy into power systems due to their straightforward control scheme, established PLL technology, and ability to operate at a specific current. However, the PLL can cause instability issues in the grid, especially when the grid impedance is high [16], [17]. With the increasing replacement of synchronous generators by PECs, this problem is becoming more prevalent and challenging. Consequently, there is a growing focus on GFM inverters, which exhibit synchronous generator-like characteristics and can operate in weak grids without relying on rigid voltage sources or forming independent grids [9], [11], [18], [19]. Furthermore, GFM inverters can address grid instability issues, including significant frequency fluctuations caused by low inertia and uncertainty in distributed energy resources. Hence, the shift towards converter-based generation necessitates accurate PEC models for assessing system dynamics that were previously ignored in conventional power systems. Therefore, modeling of GFM inverters plays a vital role in studying system-level dynamics.

For precise modeling of PECs, a comprehensive understanding of multiple aspects of the converter is necessary. This includes knowledge of its physical topology, intricate models of voltage/current control loops, PLL models, employed protection schemes, etc. [20]. Despite the known control architecture, these factors and control parameters exhibit significant variations across different manufacturers. This variability can lead to inaccurate modeling and simulation of power systems, resulting in flawed analysis and erroneous outcomes. The availability of accurate converter models is crucial for predicting system instability, ensuring component compatibility [21], and facilitating proper design of controllers and protection systems.

Modeling converter-based generation is further complicated by the need to comply with grid interconnection requirements and changes in grid codes. Manufacturers can address these requirements by modifying the control structure through software or firmware updates. For example, according to the IEEE 1547 standard, converters can actively contribute to voltage and frequency support through advanced control functions [22], [23]. This introduces an additional layer of complexity in modeling these converter systems. Data-driven models can be employed to address the aforementioned challenges. Recent advancements in data-driven modeling for GFL inverters, as discussed in the literature [18], [20], [21], [24], [25], [26], [27], primarily focus on system analysis purposes. However, the literature presents a lack of research concerning data-driven dynamic modeling techniques applied to GFM inverters operating under droop control strategies. Therefore, this paper presents a novelty by developing a data-driven modeling approach for GFM inverters.

The main objective of this paper is to develop a data-driven modeling (DDM) approach that utilizes designed probing signals to extract an underlying mathematical representation of the dynamics of a GFM inverter. System identification (SysId) methods are employed to obtain the GFM inverter DDM operating in droop mode. Additionally, an analytical approach is also derived for the GFM inverter DDM. The obtained dynamic models from both the analytical approach and the data-driven approach are then cross-validated to

ensure their power sharing capability, along with virtual and physical GFM inverters.

The novel contributions of this paper are as follows:

1) Formulated an analytical approach to derive a mathematical model describing the dynamics of GFM inverters;
2) Developed an experimental power-hardware-in-the-loop (PHIL) methodology for data collection, wherein the load connected to the GFM inverter is excited using designed probing signals. A DDM approach is designed to extract mathematical models of GFM inverter dynamics. The mathematical model is obtained by collecting output frequency and voltage data from the GFM inverter in response to changes in the active and reactive power of the load at the point of common coupling (PCC).

The paper is organized as follows: An overview of different data-driven modeling of PECs are presented in Section II. In Section III, the theoretical background on the dynamics modeling of PECs and system identification is provided. The analytical approach for modeling a system with two GFM inverter are presented in Section IV followed by data-driven approach to access the GFM inverter dynamics in Section V. In Section VI, the experimental setup to evaluate the performance of GFM inverter is discussed. The results are presented in Section VII followed by the main conclusions in Section VIII.

II. RELATED WORK ON DATA-DRIVEN MODELING APPROACHES FOR POWER ELECTRONIC CONVERTERS AND THEIR LIMITATIONS

PECs for grid integration of renewable energy sources can consist of multiple and different cascaded and interconnected converters [3]. The non-linearity of the switches used in these power electronic systems greatly increases the complexity of models. Detailed models of these converters are often used to perform accurate electromagnetic transient simulations. Though accurate, the complexity of these models are prohibitive to be used for long-term and/or large-scale system studies [28]. Furthermore, the parameters to accurately represent the exact dynamics are difficult to obtain and these methods cannot be employed without knowledge of the topology and control architecture used. In cases where the switching dynamics are neglected, averaging techniques (specifically state-space modeling techniques) are often employed to derive small-signal transfer function (TF) models [29]. However, depending on the analysis required, even such state-space models may be computationally prohibitive [28], [30].

Substantial efforts have been made to model the dynamics of such systems [21], [31], [32], [33]. Detailed models can be developed using techniques such as average state-space modeling [31], [33]. These models are very accurate and useful for component and converter level design [24], [28], but they require detailed information about the converters [33], which are often proprietary for commercial converters [32]. Even if some of the internal parameters are known, the converter properties and dynamics may have a wide range of variation depending on load requirements, battery state-of-charge, and renewable energy availability. For these reasons, developing simplified models can be beneficial [28].

Data-driven modeling (or black-box modeling) is a useful method for modeling PECs for system level studies [21], [34]. Black-box models can be developed with little-to-no information about the control or topology of a converter. As an additional benefit, black-box models usually require lower computational power compared to more detailed component level models [24]. Linear time-invariant black-box models are often designed using regression analysis and curve fitting (described with more detail in [35]). Artificial neural networks and other machine learning methods can also be used to create black-box models [24]. Tools such as those provided by MATLAB's System Identification [36] are widely used for black-box modeling. The available modeling approaches range from simple linear models based on TFs to non-linear models using approaches such as the Hammerstein-Wiener model [35], [37]. Black-box modeling of DC-DC converters has been widely explored in the literature [38], [39] and more recently for DC-AC converters [21], [31], [32], [33]. However, black-box models alone are not always accurate for a wide range operation [21]. This variation over a wide operating range can be addressed by combining multiple models to cover the dynamics over the range-of-interest [20], [21], [32].

Data-driven modeling techniques from literature have mostly focused on the converters operating in standalone mode. These models may not be suitable when the converters actively forming the grid or interact with the grid and participate in grid ancillary services, such as providing voltage and frequency support. This is especially concerning for low-inertia power systems, where PECs will have a larger share of voltage and frequency control. Hence, we are proposing a probing signal-based data-driven modeling of GFM inverters to extract their dynamics.

III. BASIC CONCEPTS OF DYNAMIC MODELING OF GRID-FORMING INVERTER AND SYSTEM IDENTIFICATION

The dynamic modeling of a GFM inverter with their control mechanism is introduced in this section, which is followed by a basic description of SysId to obtain accurate PEC dynamics.

A. POWER CIRCUIT OF GFM INVERTERS

The power circuit of i^{th}, 3-ϕ H-bridge GFM inverter consists of six switches distributed among three legs as shown in Fig. 1. The GFM is connected to the grid at PCC with voltage, $v_{\text{PCC}}^{\text{abc}}$, via an LCL filter ($L_{\text{f,i}}$, $C_{\text{f,i}}$, $L_{\text{g,i}}$) and associated equivalent series resistances ($R_{\text{f,i}}$ and $R_{\text{g,i}}$ of inductors) and a coupling line with line parameters, $L_{\text{line,i}}$, $R_{\text{line,i}}$. A dq-frame multi-loop controller is employed that generates modulated voltage vector signal, $m_{\text{i}}^{\text{abc}}$, to pulse-width modulation (PWM) controller to generate

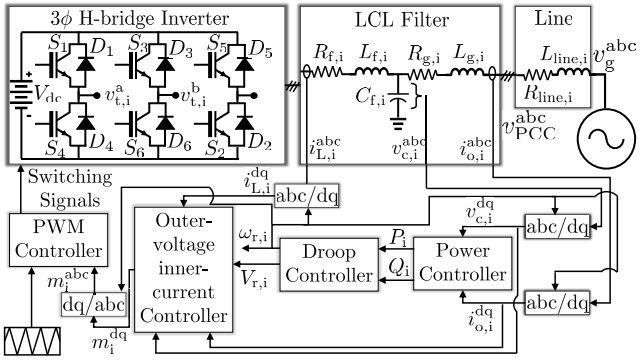

FIGURE 1. Diagram of the power circuit of i^{th} GFM inverters connected to a grid.

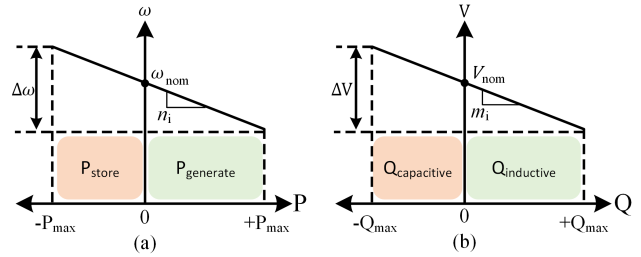

FIGURE 3. Droop control strategies. (a) *P-ω* droop (b) *Q-V* droop. *P-ω* droop control adjusts the active power output of a GFM inverter based on changes in frequency, maintaining a stable grid. *Q-V* droop control modifies the reactive power output according to variations in voltage, ensuring voltage stability in the grid.

switching signals resulting in terminal voltages, $v^{\text{a}}_{\text{t,i}}$, $v^{\text{b}}_{\text{t,i}}$ and $v^{\text{c}}_{\text{t,i}}$.

B. CONTROL OF GFM INVERTER

The control layers of the GFM inverter are illustrated in Fig. 2, depicting the various control mechanisms employed. The following sections provide a description of each control aspect of the GFM inverter.

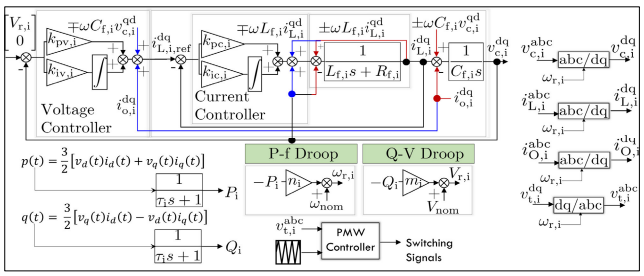

FIGURE 2. Diagram of various control loops of i^{th} GFM inverters connected to a grid.

1) POWER CONTROLLER

To determine p_{i}, and q_{i}, $v^{\text{dq}}_{\text{c,i}}$ and $i^{\text{dq}}_{\text{o,i}}$ are used. The values p_{i} and q_{i} are passed through low-pass filters with time constant, $\tau_{\text{S,i}} \in \mathbb{R}_{>0}$, to obtain P_{i} and Q_{i} as described by

$$P_{\text{i}} = [1/(\tau_{\text{S,i}}s + 1)]p_{\text{i}}, \;\; Q_{\text{i}} = [1/(\tau_{\text{S,i}}s + 1)]q_{\text{i}}, \qquad (1)$$

where $p_{\text{i}} := 1.5[v^{\text{d}}_{\text{c,i}}i^{\text{d}}_{\text{o,i}} + v^{\text{q}}_{\text{c,i}}i^{\text{q}}_{\text{o,i}}]$, $q_{\text{i}} := 1.5[v^{\text{q}}_{\text{c,i}}i^{\text{d}}_{\text{o,i}} - v^{\text{d}}_{\text{c,i}}i^{\text{q}}_{\text{o,i}}]$.

2) DROOP CONTROLLER

A droop controller in the GFM inverter is used to regulate the output frequency and voltage of the inverter to match the grid conditions. The droop controller operates by continuously monitoring the grid voltage and frequency and adjusting the inverter's output accordingly. It provides a decentralized control mechanism, allowing multiple inverters to work together and share the load in a coordinated manner. The droop controller employs a droop characteristic, which is a linear relationship between the inverter output frequency (ω) and the active power output (P), as shown in Fig. 3(a), and inverter output voltage (V) and the reactive power output (Q), as shown in Fig. 3(b). Typically, the droop characteristic is represented as a slope that determines the rate at which the frequency/voltage changes with respect to active/reactive power variations, respectively.

When the grid frequency deviates from its nominal value, the droop controller adjusts the inverter's output frequency by changing the power output proportionally to the droop slope. If the grid frequency decreases, the droop controller increases the inverter's power output, causing the frequency to rise back towards its nominal value. Conversely, if the grid frequency increases, the droop controller decreases the power output, bringing the frequency back to the desired level. The droop controller also regulates the output voltage of the inverter by monitoring the grid voltage and adjusting the inverter's voltage magnitude to maintain grid synchronization. By maintaining a stable output voltage and frequency, the droop controller ensures that the GFM inverter operates in harmony with the grid and provides reliable power supply.

Basically, droop control is a proportional controller with active and reactive power as control variables where the control gains (also the droop gains) dictate the steady–state power sharing of the inverters. The active power-frequency, *P-f*, droop control is considered here as a proportional controller (with proportional coefficient as n_{i}) with error signal $e_{\text{P,i}} := -P_{\text{i}}$ where P_{i} is the control variable. Whereas, the reactive power-voltage magnitude, *Q-V*, droop control is considered here as a proportional controller (with proportional coefficients as m_{i}) with error signal $e_{\text{Q,i}} := -Q_{\text{i}}$ where Q_{i} is the control variable. The values of n_{i} and m_{i} are typically chosen such that $\omega_{\text{r,i}}$ and $V_{\text{r,i}}$ are within the allowed specification, defined by IEEE 1547 Standard [22].

3) OUTER-VOLTAGE-INNER-CURRENT CONTROLLER

The conventional outer-voltage-inner-current controller architecture is employed for the GFM inverters [40]. For the inner-current controller, $i^{\text{dq}}_{\text{L,i,ref}}$ is provided as the reference signal to be tracked by the output signal, $i^{\text{dq}}_{\text{L,i}}$. A proportional-integral (PI) compensator is used for tracking the reference

of the dq-axis inductor current. For a desired time constant, $\tau_{c,i}$, the parameters of the current controller are selected as $k_{pc,i} = L_{f,i}/\tau_{c,i}$ and $k_{ic,i} = R_{f,i}/\tau_{c,i}$. Depending on the switching frequency, $\tau_{c,i}$ is typically selected to be in the range of 0.5-2 ms [40]. Additional feed-forward signals, $v_{c,i}^{dq}$ and $\mp\omega L_{f,i} i_{L,i}^{qd}$ facilitate the disturbance rejection capability. For the outer-voltage controller, $\begin{bmatrix} V_{r,i} & 0 \end{bmatrix}^\top$ is the reference signal to be tracked by the voltage signal, $v_{c,i}^{dq}$. A PI compensator is used to enable reference tracking. For a desired phase margin and gain cross-over frequency, the parameters of the voltage controller ($k_{pv,i}$ and $k_{iv,i}$) can be designed based on *symmetrical optimum* method [40]. Similarly, additional feed-forward signals, $v_{c,i}^{dq}$ and $\mp\omega C_{f,i} v_{c,i}^{qd}$ facilitate the disturbance rejection capability for the outer voltage control loop.

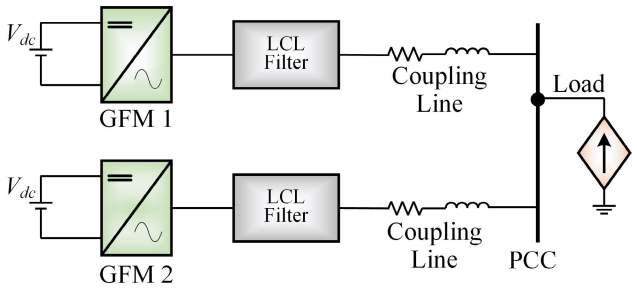

FIGURE 4. For the purpose of modeling and analysis, a system consisting of two GFM inverters is being considered. The inverter's output is directed through an LCL filter, and a load is connected to the PCC via a coupling line.

IV. ANALYTICAL MODELING OF A SYSTEM WITH TWO GFM INVERTER

The system, as shown in Fig. 4, is considered in this section for modeling and analysis. For analysis purpose, the following remarks are made:

Remark 1: The outer-voltage-inner-current control loop for GFM inverter is stable and has faster ($>$ 10 times) dynamics compared to the power and droop controller and tracks its voltage reference with minimal (assumed zero) tracking error as suggested in [40].

Remark 2: All abc-dq conversions are adopted w.r.t. GFM 1.

Using Remarks 1 and 2, the following non-linear state-space equations can be obtained for the entire system of Fig. 4:

$$\dot{\theta}_2 = \omega_{r,2} - \omega_{r,1}, \text{ where } \theta_2 := \theta_{r,2} - \theta_{r,1}, \tag{2}$$
$$\tau_{S,1}\dot{\omega}_{r,1} = \omega_{nom} - \omega_{r,1} - n_i[p_1], \tag{3}$$
$$\tau_{S,2}\dot{\omega}_{r,2} = \omega_{nom} - \omega_{r,2} - n_2[p_2], \tag{4}$$
$$\tau_{S,1}\dot{V}_{r,1} = V_{nom} - V_{r,1} - m_1[q_1], \tag{5}$$
$$\tau_{S,2}\dot{V}_{r,2} = V_{nom} - V_{r,2} - m_2[q_2], \tag{6}$$
$$L_{l,1}\dot{i}_{o,1}^{d} = V_{r,1} - R_{l,1} i_{o,1}^{d} - v_{PCC}^{d} + \omega_{r,1} L_{l,1} i_{o,1}^{q}, \tag{7}$$
$$L_{l,1}\dot{i}_{o,1}^{q} = -R_{l,1} i_{o,1}^{q} - v_{PCC}^{q} - \omega_{r,1} L_{l,1} i_{o,1}^{d}, \tag{8}$$
$$i_L^d = i_{o,1}^d + i_{o,2}^d, i_L^q = i_{o,1}^q + i_{o,2}^q \tag{9}$$

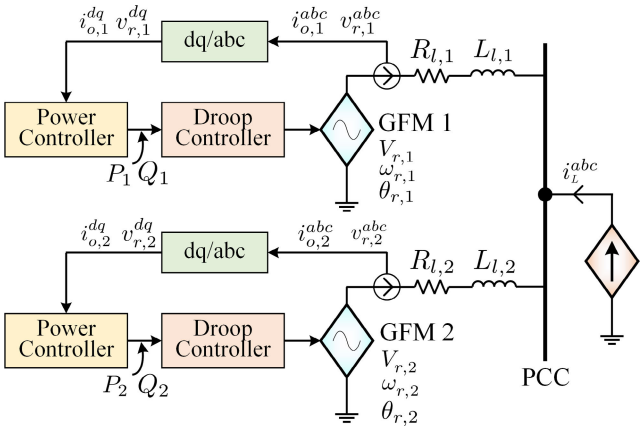

FIGURE 5. The GFM inverter is represented in the model as a voltage source that can control its phase, $\theta_{r,i}$, frequency, $\omega_{r,i}$, and amplitude. Additionally, a controlled load is connected to the PCC.

$$\begin{aligned} v_{PCC}^{d} = 0.5 \times [&(V_{r,1} + V_{r,2}\cos\theta_2) \\ &- (R_{l,1} i_{o,1}^{d} + R_{l,2} i_{o,2}^{d}) \\ &+ (\omega_{r,1} L_{l,1} i_{o,1}^{q} + \omega_{r,2} L_{l,2} i_{o,2}^{q})] \end{aligned} \tag{10}$$
$$\begin{aligned} v_{PCC}^{q} = 0.5 \times [&(V_{r,2}\sin\theta_2) - (R_{l,1} i_{o,1}^{q} + R_{l,2} i_{o,2}^{q}) \\ &- (\omega_{r,1} L_{l,1} i_{o,1}^{d} + \omega_{r,2} L_{l,2} i_{o,2}^{d})], \end{aligned} \tag{11}$$

where $\theta_{r,i}$ is the GFM inverter internal phase angle, $p_i := 1.5[V_{r,i} i_{o,i}^{d} \cos\theta_i + V_{r,i} i_{o,i}^{q} \sin\theta_i]$, $q_i := 1.5[-V_{r,i} i_{o,i}^{q} \cos\theta_i + V_{r,i} i_{o,i}^{d} \sin\theta_i]$, and ω_{nom} and V_{nom} are nominal frequency and voltage, respectively. This results in a 7$^{\text{th}}$-order non-linear electromagnetic transients (EMT) model, allowing the GFM inverter to be modeled as a voltage source with controllable phase, $\theta_{r,i}$, frequency, $\omega_{r,i}$, and amplitude, $V_{r,i}$ [41], as shown in Fig. 5.

While two GFM inverters are connected in parallel supplying a load, the system can be modeled by a non-linear system, $\dot{\underline{x}}_{GFM} = \underline{\mathcal{G}}_{GFM}(\underline{x}_{GFM})$, where, $\underline{\mathcal{G}}_{GFM}(.)$ consists of equations (2)-(11). Considering the system linearized around an equilibrium point, $\underline{x}_{GFM}^{eq}$, such that

$$\Delta\dot{\underline{x}}_{GFM} = \mathbf{A}_{GFM}\Delta\underline{x}_{GFM} + \mathbf{B}_{GFM}\Delta\underline{u}_{GFM}$$
$$\Delta\dot{\underline{y}}_{GFM} = \mathbf{C}_{GFM}\Delta\underline{x}_{GFM}$$

and

$$\mathbf{A}_{GFM} = \underline{\mathcal{F}}_{GFM}(\underline{x}_{GFM}^{eq})$$
$$\mathbf{B}_{GFM} = \begin{bmatrix} R_{l,1} & \omega_{r,1} L_{l,1} \\ -\omega_{r,1} L_{l,1} & R_{l,1} \end{bmatrix}$$
$$\mathbf{C}_{GFM} = \begin{bmatrix} 0 & 1 & 0 & 0 & 0 & 0 & 0 \\ 0 & 0 & 0 & 1 & 0 & 0 & 0 \end{bmatrix},$$

where $\underline{\mathcal{F}}_{GFM}(.)$ is the vector field of $\mathcal{G}_{GFM}(\underline{x}_{GFM})$. Here,

$$\Delta\underline{x}_{GFM} = [\Delta\theta_2\ \Delta\omega_{r,1}\ \Delta\omega_{r,2}\ \Delta V_{r,1}\ \Delta V_{r,2}\ \Delta i_{o,1}^{d}\ \Delta i_{o,1}^{q}]^\top$$
$$\Delta\underline{y}_{GFM} = [\Delta\omega_{r,1}\ \Delta V_{r,1}]^\top$$
$$\Delta\underline{u}_{GFM} = [\Delta i_L^d\ \Delta i_L^q]^\top$$

Therefore, the multiple input multiple output linearized system can be written as:

$$\begin{bmatrix}\Delta\omega_{r,1}\\ \Delta V_{r,1}\end{bmatrix} = \underbrace{\begin{bmatrix}T_1 & T_2\\ T_3 & T_4\end{bmatrix}}_{\mathbf{T}}\begin{bmatrix}\Delta i_L^d\\ \Delta i_L^q\end{bmatrix},$$

where $\mathbf{T} = \mathbf{C}_{\text{GFM}}[s\mathbf{I} - \mathbf{A}_{\text{GFM}}]^{-1}\mathbf{B}_{\text{GFM}}$ is the required TF model obtained from the analytical approach.

V. DATA-DRIVEN APPROACH TO ACCESS THE GFM INVERTER DYNAMICS

A. DATA-DRIVEN APPROACH TO ACCESS THE INVERTER DYNAMICS

1) SYSTEM IDENTIFICATION OF POWER ELECTRONIC CONVERTER

SysId is the process of obtaining a mathematical model of an unknown (dynamic) system based on applied inputs and the corresponding measured output response data. Without knowing the actual control structure and/or control parameters, a mathematical model of a PEC that captures the dynamics of interest can be estimated by using the instrument variable method.

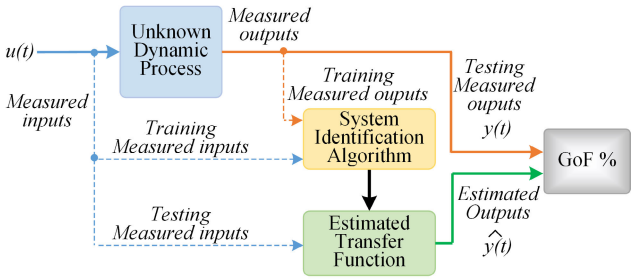

FIGURE 6. The fundamental concept of SysId. To identify the unknown dynamic process, the SysId method utilizes input and output measurements. The GoF is then calculated by comparing the actual outputs and estimated outputs.

The basic concept of a SysId process is illustrated in Fig. 6. The time domain input data $u(t)$ and time domain output data $y(t)$ from the unknown dynamic systems to be identified are first measured. The dataset is then divided into training and testing datasets. The training dataset is fed to the SysId algorithm, which estimates the system parameters (i.e., TF coefficients) by minimizing a defined cost function (in this case, the least-square error). From the estimated parameters, a TF is obtained which is then validated on the testing dataset. Finally, goodness-of-fit (GoF) based on normalized root-mean-square-error (NRMSE) is calculated to check the accuracy of the TF.

The relationship between the input and output that can be defined as:

$$y(t) + a_1 y(t-1) + \cdots + a_n y(t-n) = b_1 u(t-1) + \cdots + b_m u(t-m), \quad (12)$$

where n and m represent the number of poles and zeros of the system, respectively. Similarly, a_n and b_m represent the parameters of the difference equation of (12) or the coefficients of the equivalent TF. Then, in general, a dynamic system can be represented as:

$$\hat{y}(t \mid \theta) = [\phi(t)]^T \theta. \quad (13)$$

In (13), θ represents the set of the unknown parameters/coefficients of the system, and $\phi(t)$ represents the set of inputs $u(t)$ and outputs $y(t)$ of the dynamic system defined as follows:

$$\theta = [a_1, \ldots, a_n, b_1, \ldots, b_m]^T \quad (14)$$

$$\phi(t) = [-y(t-1) \cdots - y(t-n)\, u(t-1) \ldots u(t-m)]^T \quad (15)$$

Now, if we define Z^N as the set of known measurements and N is overall input-output data in the time interval $1 \le t \le N$:

$$Z^N = \{u(1), y(1), \ldots, u(N), y(N)\}, \quad (16)$$

then the unknown parameters of the system, θ, can be estimated by employing a least-squares method utilizing the following cost-function [35]:

$$\underset{\theta}{\text{minimize}}\, V_N\left(\theta, Z^N\right), \quad (17)$$

where

$$V_N\left(\theta, Z^N\right) = \frac{1}{N}\sum_{t=1}^{N} \left\|y(t) - \hat{y}(t \mid \theta)\right\|^2. \quad (18)$$

Based on the collected input-output data, a set of models with different numbers of poles and zeros can be fit to the data. The GoF of each model can be calculated using NRMSE as in (19), defined as [36]:

$$\text{GoF} = 100 \times \left(1 - \frac{\left\|y(t) - \hat{y}(t)\right\|_2}{\left\|y(t) - \text{mean}\, y(t)\right\|_2}\right), \quad (19)$$

where $\|.\|_2$ indicates the 2-norm.

2) PROBING SIGNALS

When parameterizing a DDM, using properly designed probing signals to perturb the system response plays a crucial role in understanding system behavior [42]. Simultaneously, the probing signal must be designed within the constraints imposed by the power system and SysId theory [43], which involves placing the probing signal content within the frequency band of interest by application without disrupting the power system operations. Additionally, since the system may have different time constants, using rectangular/square probing signals are ideal for accurately estimating time constant and emphasizing a particular frequency range based on signal frequency [42], [44]. In [27], four different probing signals were compared, and logarithmic square chirp was found to be the most accurate for extracting the dynamics of PECs. Therefore, in the current research, logarithmic square chirp — a signal that involves logarithmically sweeping the frequency of a square wave signal — will be used to perturb

the system. The signal that is used in the research has the following fundamental explanation:

$$x(t) = A \times \text{square}(\omega t). \tag{20}$$

Here, A represents the peak amplitude of the square wave, while ωt denotes the phase angle, which is modified using the trapezoidal method as shown in the following Eq. 21.

$$(\omega t)_k = (\omega t)_{k-1} + \frac{t_k - t_{k-1}}{2} \times 2 \times \pi \times (f_{(t_k)} + f_{(t_{k-1})}) \tag{21}$$

Here, k denotes the discrete time instant (where $k-1$ refers to the previous time instant), $(\omega t)_{k-1}$ and $(\omega t)_k$ correspond to the phase angle at the previous and current time respectively. Additionally, t_{k-1} and t_k represent the time at the previous and current time instant respectively, while $f_{(t_k)}$ and $f_{(t_{k-1})}$ denote the frequency at time t_k and t_{k-1} respectively.

Similarly, the frequency $f_{(t_k)}$ is defined as in (22):

$$f_{(t_k)} = f_0 \times \left(\left(\frac{f_0}{f_1} \right)^{\frac{1}{T}} \right)^{t_k}, \tag{22}$$

where f_0, f_1, and T denote the starting frequency, final frequency, and duration of the chirp signal, respectively.

3) DESIGN CRITERIA OF CHIRP SIGNAL

According to the basic description of the signal, this paper presents the design parameters of the chirp signal as f_0, f_1, T, and A.

a: FINAL FREQUENCY (F_1)

The parameter f_1 in a chirp signal is the final frequency at which the signal has the shortest duration of constant value, also known as the minimum hold time T_h. However, it is important to choose an appropriate value for T_h, not too small or too large; if it is too small, the system does not have enough time to stabilize, and the resulting model would not accurately describe the system's static behavior. On the other hand, if it is too large, the model will overemphasize low frequencies and leave gaps in the input data, making it difficult for the model to accurately capture the system's behavior in those regions. Therefore, it is recommended to set T_h to be approximately equal to the system's time constant (τ_{system}) [42]. Thus, the final frequency of the signal can be calculated as in (23):

$$f_1 \approx \frac{1}{2 \times T_h} \approx \frac{1}{2 \times \tau_{system}}. \tag{23}$$

The reason for multiplying (23) by 2 is to account for both the ON and OFF time of the signal. To determine the value of τ_{system}, a step input is applied to the system and the settling time t_s is measured. The value of τ_{system} can then be calculated based on the chosen tolerance band as in [45]:

$$\tau_{system} = \frac{t_s}{3} \quad \text{(for 5\% tolerance band)}$$

or

$$\tau_{system} = \frac{t_s}{4} \quad \text{(for 2\% tolerance band)}.$$

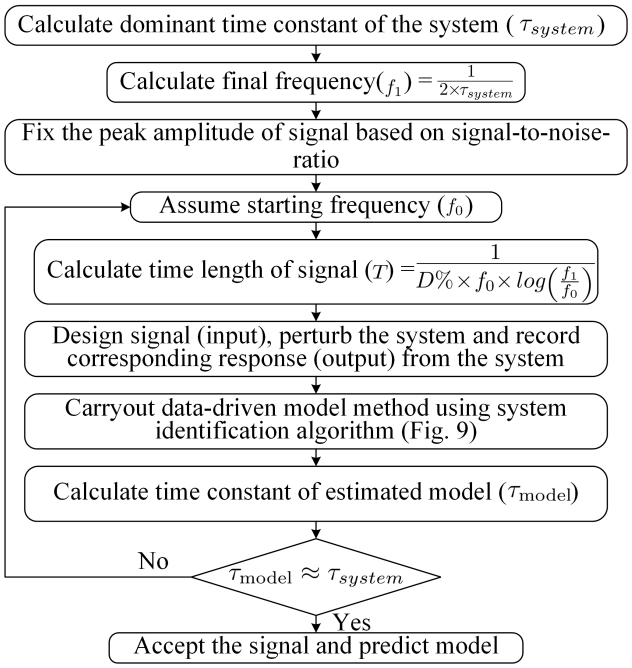

FIGURE 7. Flowchart to design probing signal for SysId.

b: STARTING FREQUENCY (F_0)

The minimum frequency of a chirp signal is represented by f_0. It is determined through an iterative process and requires updating in each iteration until the value of τ_{model} matches that of τ_{system}, as shown in Fig. 7.

c: TIME LENGTH OF SIGNAL (T)

The time duration of the chirp signal is denoted as T and represents the time elapsed between two specific instantaneous frequencies f_0 and f_1. This value can be expressed as shown in [46] and can be calculated as in (24):

$$T = \frac{1}{D\% \times f_0 \times log\left(\frac{f_1}{f_0}\right)}, \tag{24}$$

where D is the percentage rate of exponential change in frequency of the signal.

d: PEAK AMPLITUDE OF SIGNAL (A)

The amplitude of the square chirp signal is denoted by A and its value depends on the signal-to-noise ratio of the system [47], which can vary. The selection of A should be done carefully so that the output signal has the minimum possible noise after applying the designed signal to the system. If A is not chosen properly, additional filters may be required to eliminate noise, which will be discussed in more detail in Section VII. The flowchart of designing the probing signal for DDM parameterization is illustrated in Fig. 7.

B. PARTITIONED MODELING OF DROOP CONTROLLER

Due to the presence of nonlinearities in GFM inverters, modeling of GFM inverter with droop controller over the

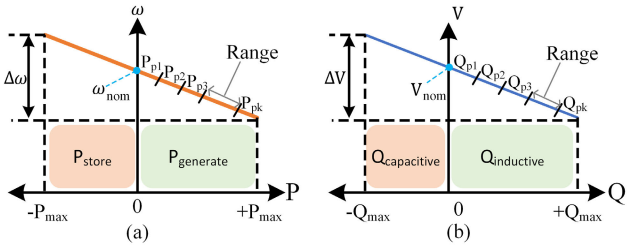

FIGURE 8. Demonstration of linear partitioning of the GFM inverter. The *P-ω* and *Q-V* droop curve are divided into several ranges.

operating regions results in intricate dynamic models, and the complex dynamics of the whole operating region are effectively captured by dividing the operating regions further into small linear ranges [20], [48], as shown in Figs. 8(a) and 8(b), where $P_{p1}, P_{p2}, \ldots, P_{pk}$ represent ranges corresponding to load active power changes, and $Q_{q1}, Q_{q2}, \ldots, Q_{qk}$ represent ranges associated with load reactive power changes.

Algorithm 1 Active Power Variation to Generate Probing Signal for Frequency Variation

Input: Operational limits $\leftarrow [P_{low}, P_{max}]$
Simulation clock time $\leftarrow t$
Initialization:
Time interval for each partition $\leftarrow T$
Lower active power starting value $P_{k1} \leftarrow P_{low}$
Higher active power for same partition P_{k2}
Difference between active power $dp \leftarrow P_{k2} - P_{k1}$
while *True* **do**
  $k \leftarrow \text{floor}(t/T)$
  $p_1 \leftarrow P_{k1} + k \times dp/2$
  $p_2 \leftarrow p_1 + dp$
  if $p_2 > P_{max}$ **then**
    $p_1 \leftarrow P_{max} - dp$
    $p_2 \leftarrow P_{max}$
  end
end

With the selected operating limits, the desired active power signal is generated according to Algorithm 1 to extract reduced-order linear dynamic models of the GFM inverter for frequency variations. Additionally, the reactive power signal is generated based on Algorithm 2 to obtain reduced-order linear dynamic models of the GFM inverter for voltage variations.

C. FLOWCHART TO ASSESS GRID-FORMING INVERTER DYNAMICS

The flowchart to identify the TF of a GFM inverter from the SysId algorithm is shown in Fig. 9. Logarithm square-chirp probing signal is used to perturb the load to extract dynamics of PECs [27]. Fig. 10 shows the load active power variation, which is varied from 0 to 20 kW for 15 seconds, after which it is increased by 10 kW in subsequent ranges until reaching

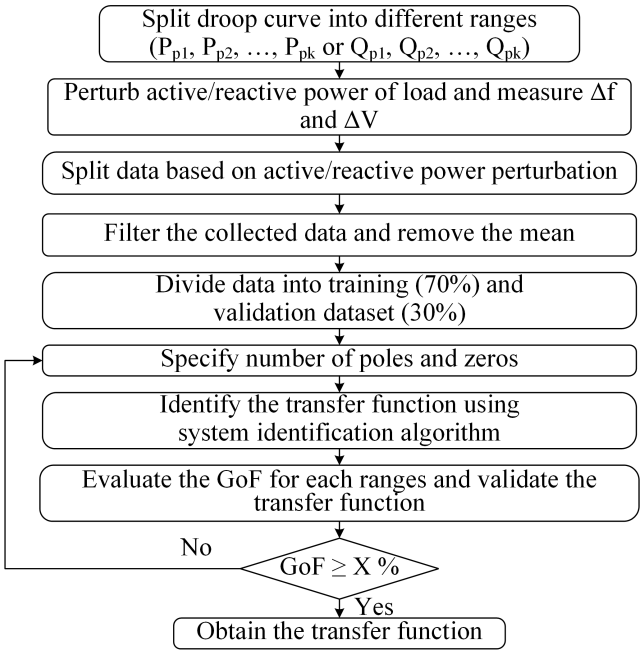

FIGURE 9. Flowchart to identify TF using SysId.

Algorithm 2 Reactive Power Variation to Generate Probing Signal for Voltage Variation

Input: Operational limits $\leftarrow [Q_{low}, Q_{max}]$
Simulation clock time $\leftarrow t$
Initialization:
Time interval for each partition $\leftarrow T$
Lower reactive power starting value $Q_{k1} \leftarrow Q_{low}$
Higher reactive power for same partition Q_{k2}
Difference between reactive power $dq \leftarrow Q_{k2} - Q_{k1}$
while *True* **do**
  $k \leftarrow \text{floor}(t/T)$
  $q_1 \leftarrow Q_{k1} + k \times dq/2$
  $q_2 \leftarrow q_1 + dq$
  if $q_2 > Q_{max}$ **then**
    $q_1 \leftarrow Q_{max} - dq$
    $q_2 \leftarrow Q_{max}$
  end
end

a total of 200 kW. This power variation follows the droop curve characteristics of the GFM inverter. The frequency of the square-chirp signal ranges from 1 Hz to 32 Hz, with values selected based on the settling time response parameters of the GFM inverter. Similarly, Fig. 11 illustrates the load reactive power variation, which is varied from 0 to 20 kVAr for 15 seconds, and then increased by 10 kVAr in subsequent ranges until reaching a total of 200 kVAr. This reactive power adjustment aligns with the droop curve characteristics of the GFM inverter.

To determine the TF of a commercially available 3-ϕ, 480 V, 60 Hz, 125 kVA Dynapower GFM inverter [49]

TABLE 1. Transfer functions of GFM 1 inverter obtained from both analytical and data-driven approach.

Transfer Functions Obtained From Analytical Approach	
$T_{1\_Analytical} = \text{TF}(\frac{\omega}{i_{Ld}})$	$\frac{-0.00352s^5-12.21s^4-1189s^3-3.887e04s^2-4.247e05s-4.977e04}{s^7+6789s^6+1.207e07s^5+1.494e09s^4+7.191e10s^3+1.986e12s^2+3.887e13s+3.986e14}$
$T_{2\_Analytical} = \text{TF}(\frac{\omega}{i_{Lq}})$	$\frac{0.0003977s^5+0.03122s^4-809.7s^3-4.942e04s^2-7.558e05s-8.884e04}{s^7+6789s^6+1.207e07s^5+1.494e09s^4+7.191e10s^3+1.986e12s^2+3.887e13s+3.986e14}$
$T_{3\_Analytical} = \text{TF}(\frac{v}{i_{Ld}})$	$\frac{0.01909s^5+1.742s^4+54.92s^3-2.927e05s^2-1.783e07s-2.711e08}{s^7+6789s^6+1.207e07s^5+1.494e09s^4+7.191e10s^3+1.986e12s^2+3.887e13s+3.986e14}$
$T_{4\_Analytical} = \text{TF}(\frac{v}{i_{Lq}})$	$\frac{0.1689s^5+585.8s^4+5.253e04s^3+1.622e06s^2+1.854e07s+4.477e07}{s^7+6789s^6+1.207e07s^5+1.494e09s^4+7.191e10s^3+1.986e12s^2+3.887e13s+3.986e14}$
Transfer Functions Obtained From Data-driven Approach	
$T_{1\_DDM} = \text{TF}(\frac{\omega}{i_{Ld}})$	$\frac{-104.5s^5-2869s^4-1.257e05s^3-1.773e05s^2-2.56e04s-4562}{s^7+138.7s^6+1.947e04s^5+6.389e05s^4+1.721e07s^3+2.392e07s^2+3.336e06s+6.194e05}$
$T_{2\_DDM} = \text{TF}(\frac{\omega}{i_{Lq}})$	$\frac{2.539e07s^5-2.101e09s^4-2.356e10s^3-4.357e12s^2-1.233e13s-3.314e12}{s^7+421.3s^6+9.008e04s^5+8.876e06s^4+3.553e08s^3+1.165e10s^2+3.219e10s+7.277e09}$
$T_{3\_DDM} = \text{TF}(\frac{v}{i_{Ld}})$	$\frac{5.506e08s^5+2.015e10s^4+2.068e11s^3+5.602e11s^2-2.938e10s+9.118e10}{s^7+1825s^6+1.866e05s^5+1.076e07s^4+9.824e07s^3+3.272e08s^2+7.241e07s+3.568e07}$
$T_{4\_DDM} = \text{TF}(\frac{v}{i_{Lq}})$	$\frac{1175s^5+1.309e05s^4+4.178e06s^3+3.367e07s^2+2.84e07s+2.934e06}{s^7+281.7s^6+5.059e04s^5+3.255e06s^4+1.174e08s^3+8.502e08s^2+8.494e08s+1.935e07}$

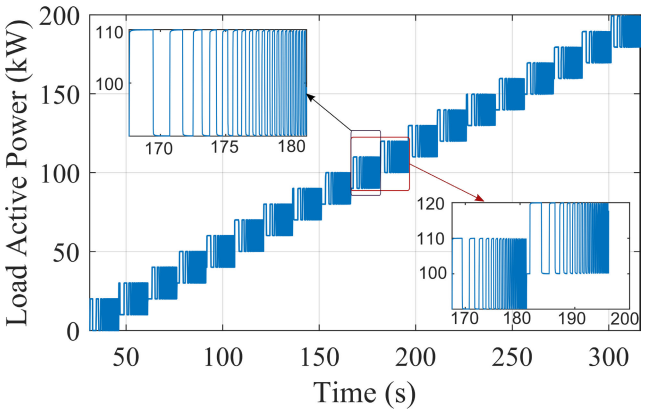

FIGURE 10. Sq-chirp probing signal, generated using Algorithm 1, was employed to excite load active power ranging from 0 to 200 kW.

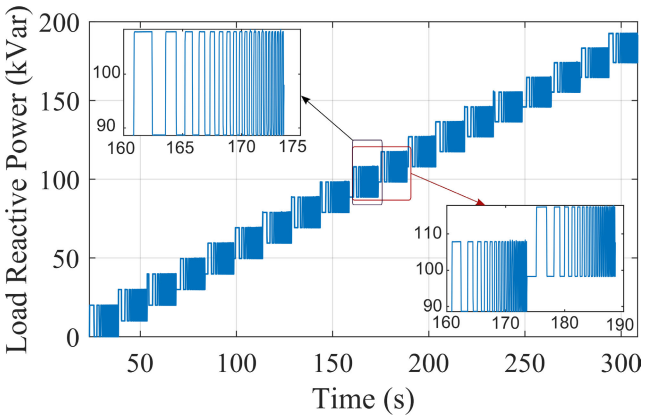

FIGURE 11. Sq-chirp probing signal, generated using Algorithm 2, was employed to excite load reactive power ranging from 0 to 200 kVAr.

(represented as GFM 1 onwards), the measured inputs, including the active and reactive power supplied by the GFM 1 and the output frequency and voltage at the terminal of the GFM 1, are logged using a real-time simulator (RTS) system from Opal-RT. The collected data is divided into small ranges for analysis. Then, the data is filtered using a mean filter to smooth the logged data. Furthermore, the mean of both active power and reactive power, and frequency and voltage of GFM 1 measurements are eliminated to obtain more accurate TF model. This allows SysId to focus on the real variations caused by the probing signals. The dataset is divided into two parts for cross-validation: a training set for computing TF model, and a validation set for validating the resulting TF model. The number of poles and zeroes of TF model for data-driven approach are chosen based on the TF finding from analytical approach.

VI. EXPERIMENTAL SETUP

The hardware experimental setup is developed as shown in Fig. 12. An ideal transformer model-based PHIL [50] setup is employed, which comprises an OP5707 RTS, an Ametek grid simulator, and GFM 1. The grid simulator utilized in this experiment was a controlled AC source amplifier with a capacity of 270 kVA. The RTS, grid simulator, and console PC were used collectively to which GFM 1 was connected. Additionally, the AV900 bidirectional DC supply, which was available in the power system integration lab at the National Renewable Energy Laboratory, was connected to the DC terminal of GFM 1. The console PC and OP5707 RTS communicated using the User Datagram Protocol (UDP) over Ethernet.

Fig. 12 is used to assess the TF of GFM 1, which includes an Opal-RT with a virtual GFM (GFM 2) and virtual load. GFM 1 is linked to the model through PHIL. The active and reactive power of the load were perturbed using a square-chirp probing signal, as shown in Figs. 10 and 11, respectively. These probing signals were used in Fig. 12 to excite the GFM inverters, which consequently affect the frequency and voltage produced by the GFM inverters. These probing signals were generated using Algorithms 1 and 2. The settings for the Ametek grid simulator, GFM 1, GFM 2, inverter filter parameter, and load are shown in the appendix in Table 2.

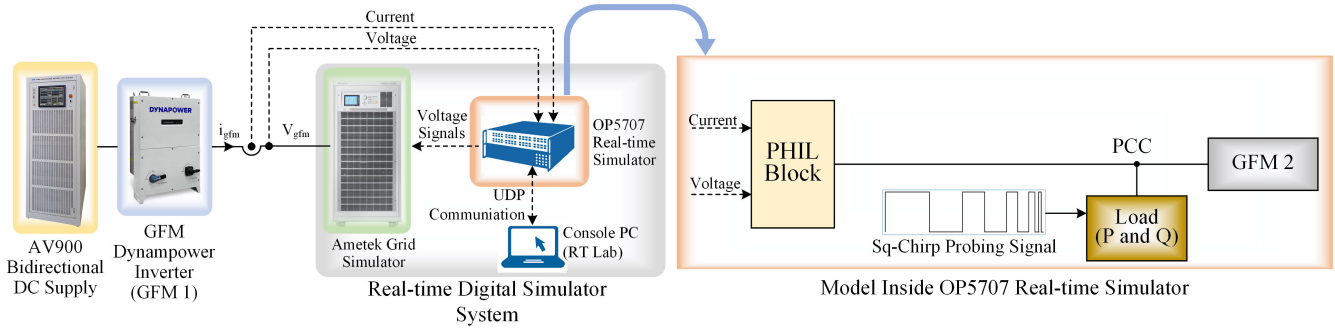

FIGURE 12. Experimental setup to assess the TF of GFM Dynapower inverter (GFM 1) as analyzed in Fig. 4. Loads *P* and *Q* are excited by the Sq-chirp probing signal.

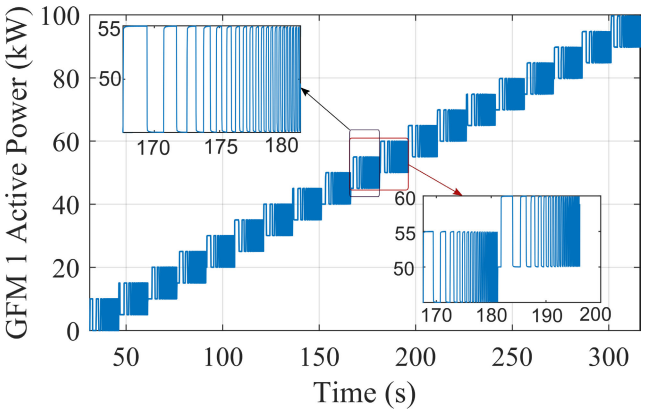

FIGURE 13. Active power supplied by GFM 1 due to perturbation of load active power.

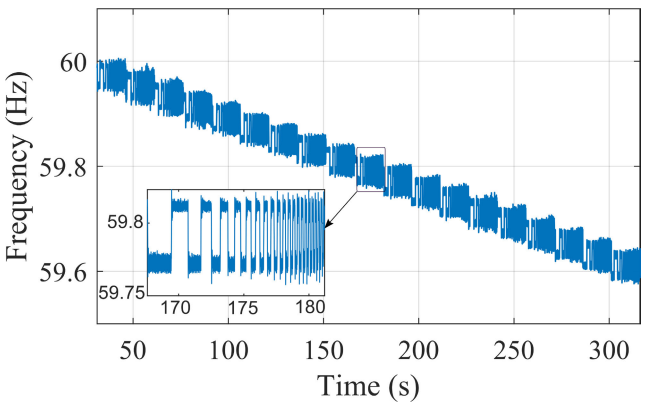

FIGURE 14. Frequency response of GFM 1 due to perturbation of load active power.

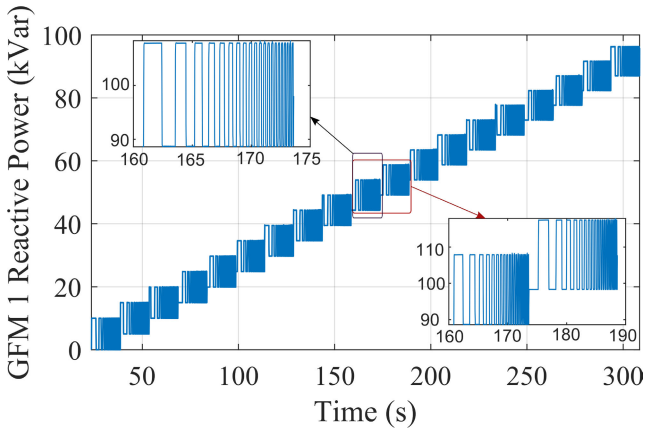

FIGURE 15. Reactive power supplied by GFM 1 due to perturbation of load reactive power.

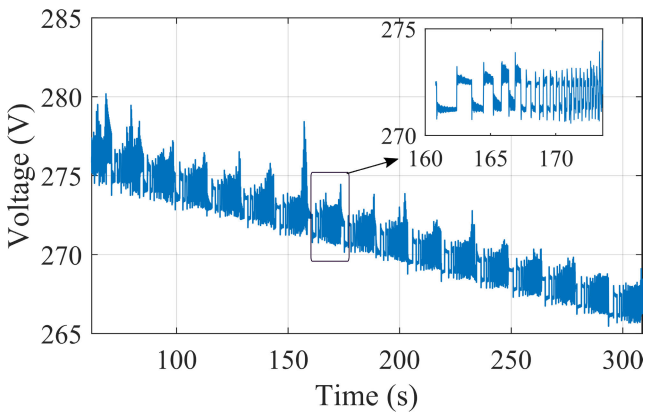

FIGURE 16. Voltage response of GFM 1 due to perturbation of load reactive power.

VII. RESULTS AND ANALYSIS

The TF of GFM 1 inverter which operates in droop mode is obtained from the SysId algorithm and the response (frequency/voltage) of GFM 1 inverter with the change in load active/reactive power are analyzed in this section.

Active power supplied by the GFM 1 inverter due to change in active power of load is depicted in Fig. 13, while GFM 1 frequency response is illustrated in Fig. 14. It can be observed that as the active power of the load increases, active power supplied by the GFM 1 inverter also increases but the frequency decreases, aligning with the droop curve characteristic of the GFM inverter. Similarly, Fig. 15 represents the reactive power supplied by the GFM 1 inverter due to the variation in the reactive power of the load, and Fig. 16 showcases the response of GFM 1 voltage. It is evident

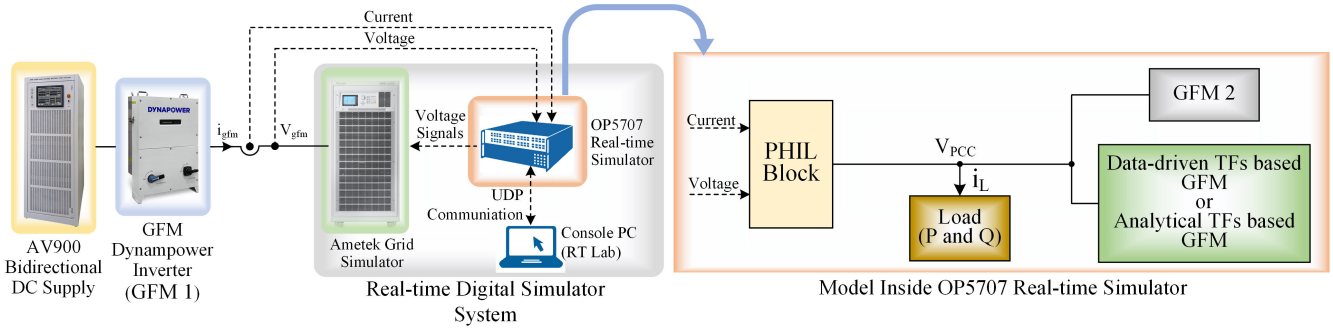

FIGURE 17. Experimental setup to validate the TFs obtained from analytical and data-driven approach of GFM 1.

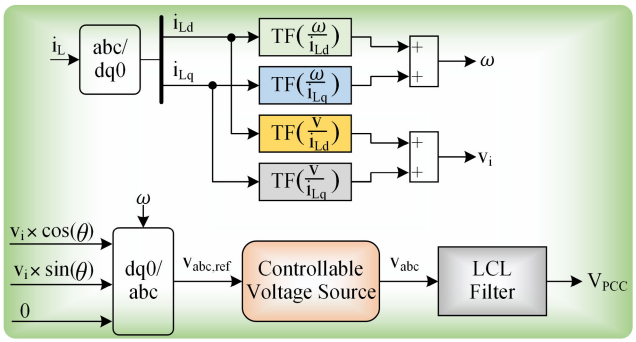

FIGURE 18. Implementation of obtained TF from analytical and data-driven approach in the EMT simulation.

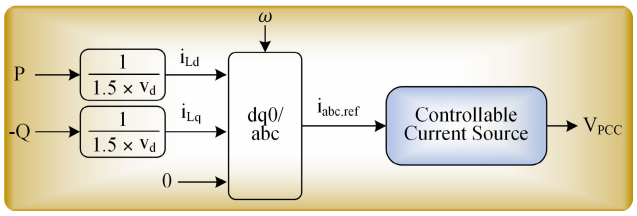

FIGURE 19. Implementation of load in the EMT simulation.

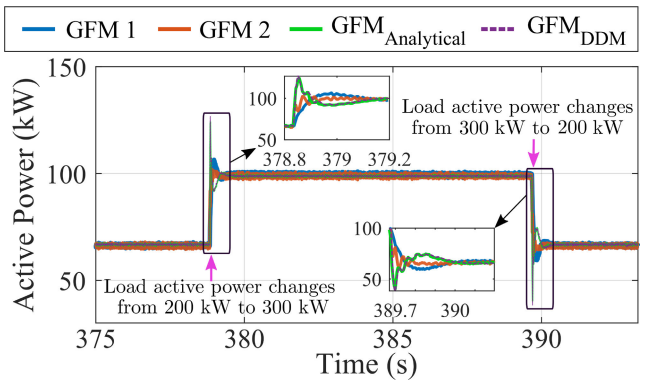

FIGURE 20. Active power shared by GFM 1, GFM 2, and TFs-based GFM obtained from the analytical and DDM approach.

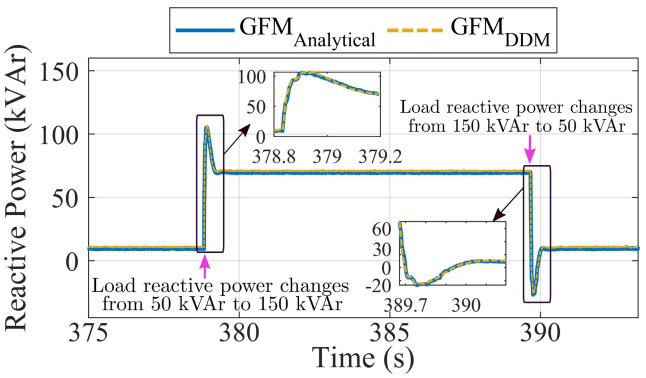

FIGURE 21. Reactive power response comparison for TFs-based GFM obtained from analytical and DDM approach.

that as the reactive power of the load increases, GFM 1 inverter supplied more reactive power which results in drop in the GFM 1 terminal voltage, aligning with the droop curve behavior of the GFM inverter. Table 1 displays the TFs corresponding to the GFM 1 inverter. These TFs were derived from analytical and data-driven modeling approach.

A. VALIDATION OF GFM 1 TF WITH ONE PHYSICAL GFM INVERTER

The validation of the GFM 1 inverter's TF, as obtained in Table 1, is subsequently incorporated into an EMT simulation using Opal-RT, as illustrated in Fig. 17. This simulation is employed to verify the power distribution among the TF-based GFM, GFM 1, and GFM 2 under different load scenarios. In Fig. 18, the TF-based GFM model is implemented in the EMT simulation using Opal-RT RTS. Here, the load current is passed to the $abc - dq0$ block, where the direct and quadrature axis currents (i_{Ld}, i_{Lq}) are calculated. These currents are fed into the TF-based GFM model, and the output of the TF-based GFM model provides estimates for voltage and frequency (v_i, ω). Subsequently, v_i is conveyed to the $dq0 - abc$ block to generate the reference voltage (V_{abc_ref}). V_{abc_ref} is then supplied to a controllable voltage source, and its output passes through an LCL filter to produce the PCC voltage (V_{PCC}).

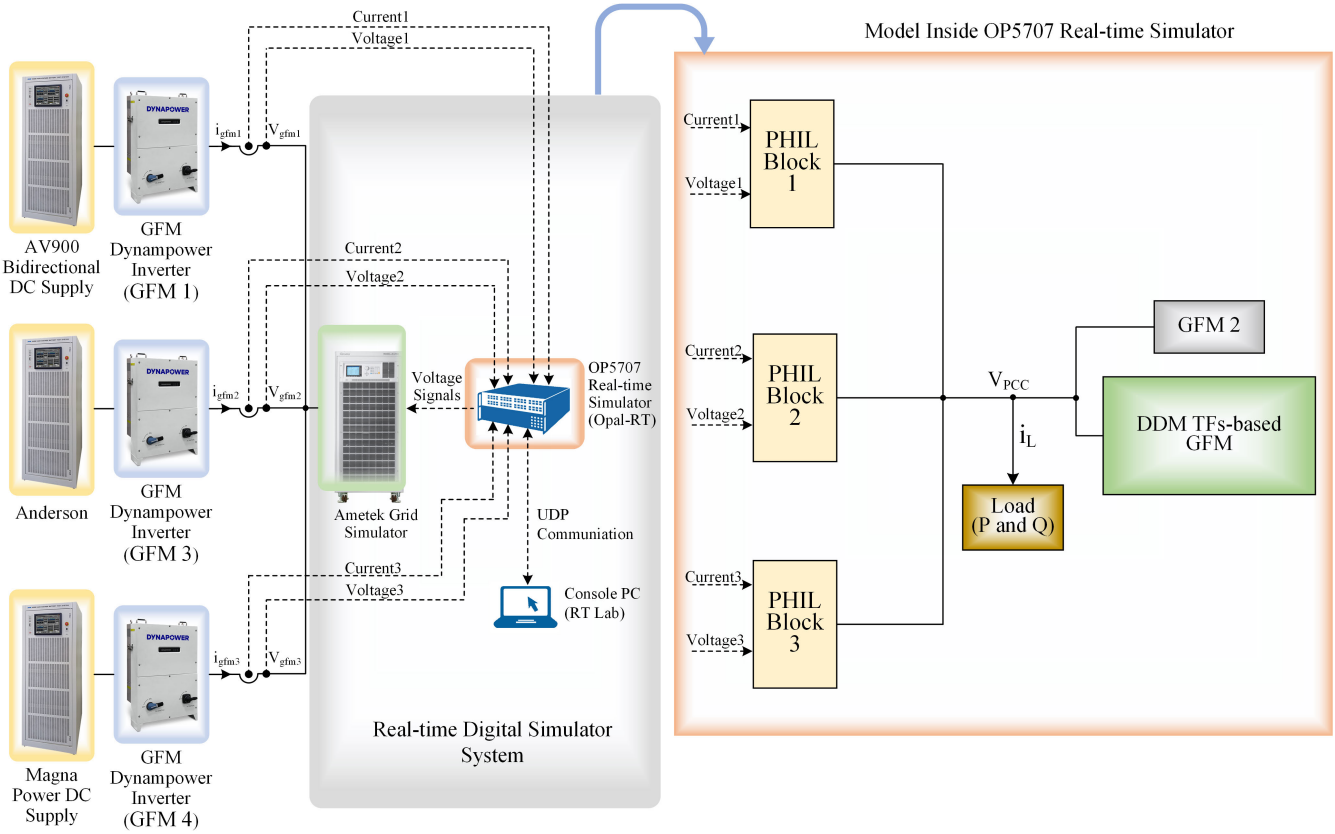

FIGURE 22. Experimental setup for validating the DDM TFs-based GFM inverter in a system with three physical GFM inverters.

Similarly, in Fig. 19, the load current (i_{Ld}, i_{Lq}) is calculated from active and reactive power (P and Q) of load, which is then passed to $abc - dq0$ block to generate the reference current (i_{abc_ref}); i_{abc_ref} is then passed to a controllable current source to generate the PCC voltage (V_{PCC}).

To validate the TFs-based GFM, initially the TF obtained through the analytical approach is implemented in Fig. 17 and then TF obtained from DDM approach is implemented. The comparison of active power shared by GFM 1, GFM 2, and TFs-based GFM obtained from analytical and DDM approaches is depicted in Fig. 20. Here, the active power of the load is changed from 200 kW to 300 kW at 378.8 sec and then reverted back to 200 kW from 300 kW at 389.7 sec. The results indicate an equal power sharing across all three GFMs. Initially, 66.67 kW of active power is shared, followed by 100 kW, and then again 66.67 kW of power distribution, corresponding to the load changes. Fig. 20 also shows that active power shared by TFs-based GFM obtained from DDM exhibits similar dynamics compared to the analytical TFs-based GFM approach. However, the dynamics is slightly different compared to GFM 1 dynamics. This difference might be due to the challenge of capturing some of the non-linearities of the GFM 1 inverter dynamics that are not being fully captured in this large signal event, which is a limitation for the current implementation of this method that should be addressed as future work. However, both models converged in steady state with the GFM 1 and GFM 2 implementations. To compare the performance of TFs-based GFM obtained from the analytical and DDM approaches, GoF based on NRMSE as given in Eq. 19 is calculated. For this, active power supplied from both the TF-based GFM models is compared with the GFM 1 active power. The GoF for the analytical approach and data-driven approach is calculated to be 89.09% and 87.97% respectively. This demonstrates that both approaches can accurately capture the dynamic response of GFM inverters under different loading conditions.

Similarly, in Fig. 21, we compare the reactive power responses of the TFs-based GFM obtained from the analytical and DDM approaches. The reactive power of the load is changed from 50 kVAr to 150 kVAr at 378.8 sec and then reverted back to 50 kVAr from 150 kVAr at 389.7 sec. The DDM TFs-based GFM approach exhibits similar dynamics compared to analytical TFs-based GFM approach.

B. VALIDATION OF GFM 1 TF WITH THREE PHYSICAL GFM INVERTERS

The validation of the TFs-based GFM obtained from DDM with three physical GFM inverter is illustrated in Fig. 22. The experimental hardware setup involves three physical Dynapower GFM inverters, specifically GFM 1, GFM 3, and GFM 4. The RTS, grid simulator, and console PC were

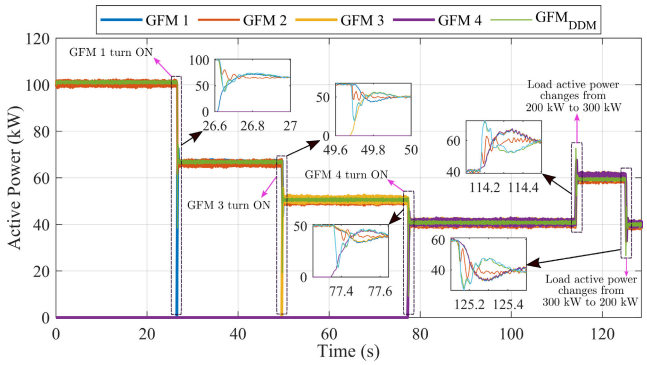

FIGURE 23. Active power shared by GFM 1, GFM 2, GFM 3, GFM 4, and TFs-based GFM obtained from the analytical and DDM approach.

collectively employed to connect GFM 1, GFM 3, and GFM 4 in the EMT simulation. Utilizing three PHIL blocks, these inverters were interconnected with the EMT simulation. This arrangement facilitates the integration of GFM 2, TFs-based DDM GFM inverter, and the load into the system. The grid simulator utilized in this experiment was a controlled AC source amplifier with a capacity of 270 kVA. Additionally, the AV900 bidirectional DC supply, Anderson, and Magna Power DC supply which were available in the power system integration lab at the National Renewable Energy Laboratory, were connected to the DC terminal of GFM 1, GFM 3, and GFM 4 respectively. The console PC and OP5707 RTS communicated using the UDP over Ethernet.

The comparison of active power shared by GFM 1, GFM 2, GFM 3, GFM 4, and DDM TFs-based GFM is depicted in Fig. 23. During start-up, none of the physical GFM inverters are connected to the Opal-RT simulation model. Thus, 200 kW load power is shared by GFM 2 and DDM TFs-based GFM (Each GFM injecting 100 kW active power). At time 26.6 sec, 49.6 sec, and 77.4 sec, GFM 1, GFM 3, and GFM 4 are connected to the EMT simulation, resulting an equal power sharing of 66.67 kW, 50 kW, and 40 kW respectively across all GFMs. When all the GFM inverters are connected, the active power of the load is changed from 200 kW to 300 kW at 114.2 sec and then reverted back to 200 kW from 300 kW at 125.2 sec. The results indicate an equal power sharing across all five GFMs. Initially, 40 kW of active power is shared, followed by 60 kW, and then again 40 kW of active power, corresponding to the load changes.

VIII. CONCLUSION

This paper presents an analytical approach and DDM approach to obtain mathematical model of GFM inverter dynamics. A DDM modeling approach uses PHIL experiments to capture dynamic GFM data in the application of DDM techniques. A square-chirp probing signal was employed to perturb the active and reactive power of the load inside the Opal-RT model. The dynamic response of the GFM inverter, including changes in frequency and voltage, was recorded. This data was then used in system identification algorithm to identify the dynamic models of the GFM inverter. Furthermore, the mathematical model of GFM inverter dynamics obtained from analytical approach and DDM approach are then compared based on GoF. GoF for the analytical approach and DDM approach was calculated to be 89.09% and 87.97% respectively. Hence, both approach demonstrated accuracy in capturing the dynamic response of GFM inverters under varying loading conditions.

APPENDIX

Table 2 displays the parameters related to GFM inverters (GFM 1, GFM 2, GFM 3, and GFM 4), including the droop controller parameter, inverter filter parameter, and load parameter.

TABLE 2. GFM Inverter, LCL filter, and load parameters [1].

Parameter	Value
Rated power capacity of GFM inverter	125 kVA
Frequency droop gain for GFM inverter	0.5 Hz/125 kW
Voltage droop gain for GFM inverter	24 V/125 kVAr
Nominal frequency	60 Hz
Line-line voltage	480 V
L_f	150e-6 H
R_f	50e-3 Ω
C_f	110e-6 F
L_g	15e-6 H
R_g	50e-3 Ω
Load active power change	0 - 200 kW
Load reactive power change	0 - 200 kVAr

ACKNOWLEDGMENT

The views expressed in the article do not necessarily represent the views of the DOE or the U.S. Government. The U.S. Government retains and the publisher, by accepting the article for publication, acknowledges that the U.S. Government retains a nonexclusive, paid-up, irrevocable, worldwide license to publish or reproduce the published form of this work, or allow others to do so, for U.S. Government purposes.

REFERENCES

[1] R. H. Byrne, T. A. Nguyen, D. A. Copp, B. R. Chalamala, and I. Gyuk, "Energy management and optimization methods for grid energy storage systems," *IEEE Access*, vol. 6, pp. 13231–13260, 2018.

[2] G. Venkataramanan and B. Wang, "Dynamic modeling and control of three phase pulse width modulated power converters using phasors," in *Proc. IEEE 35th Annu. Power Electron. Specialists Conf.*, Jun. 2004, pp. 2822–2828.

[3] C. Shah, J. D. Vasquez-Plaza, D. D. Campo-Ossa, J. F. Patarroyo-Montenegro, N. Guruwacharya, N. Bhujel, R. D. Trevizan, F. A. Rengifo, M. Shirazi, R. Tonkoski, R. Wies, T. M. Hansen, and P. Cicilio, "Review of dynamic and transient modeling of power electronic converters for converter dominated power systems," *IEEE Access*, vol. 9, pp. 82094–82117, 2021.

[4] P. Kundur, N. J. Balu, and M. G. Lauby, *Power System Stability and Control*, vol. 7. New York, NY, USA: McGraw-Hill, 1994.

[5] F. Milano, F. Dörfler, G. Hug, D. J. Hill, and G. Verbic, "Foundations and challenges of low-inertia systems (invited paper)," in *Proc. Power Syst. Comput. Conf. (PSCC)*, Jun. 2018, pp. 1–25.

[6] *Inverter-Based Resource Performance Issues Report*. Accessed: Nov. 2023. [Online]. Available: https://www.nerc.com/comm/RSTC_Reliability_Guidelines/NERC_Inverter-Based_Resource_Performance_Issues_Public_Report_2023.pdf

[7] X. Wang, M. G. Taul, H. Wu, Y. Liao, F. Blaabjerg, and L. Harnefors, "Grid-synchronization stability of converter-based resources—An overview," *IEEE Open J. Ind. Appl.*, vol. 1, pp. 115–134, 2020.

[8] S.-K. Chung, "A phase tracking system for three phase utility interface inverters," *IEEE Trans. Power Electron.*, vol. 15, no. 3, pp. 431–438, May 2000.

[9] Y. Li, Y. Gu, Y. Zhu, A. Junyent-Ferré, X. Xiang, and T. C. Green, "Impedance circuit model of grid-forming inverter: Visualizing control algorithms as circuit elements," *IEEE Trans. Power Electron.*, vol. 36, no. 3, pp. 3377–3395, Mar. 2021.

[10] S. D'Arco and J. A. Suul, "Equivalence of virtual synchronous machines and frequency-droops for converter-based MicroGrids," *IEEE Trans. Smart Grid*, vol. 5, no. 1, pp. 394–395, Jan. 2014.

[11] R. Rosso, X. Wang, M. Liserre, X. Lu, and S. Engelken, "Grid-forming converters: Control approaches, grid-synchronization, and future trends—A review," *IEEE Open J. Ind. Appl.*, vol. 2, pp. 93–109, 2021.

[12] S. Fazal, M. E. Haque, M. T. Arif, and A. Gargoom, "Droop control techniques for grid forming inverter," in *Proc. IEEE PES 14th Asia–Pacific Power Energy Eng. Conf. (APPEEC)*, Nov. 2022, pp. 1–6.

[13] Q.-C. Zhong, "Virtual synchronous machines: A unified interface for grid integration," *IEEE Power Electron. Mag.*, vol. 3, no. 4, pp. 18–27, Dec. 2016.

[14] M. Lu, "Virtual oscillator grid-forming inverters: State of the art, modeling, and stability," *IEEE Trans. Power Electron.*, vol. 37, no. 10, pp. 11579–11591, Oct. 2022.

[15] Y. Bae, T.-K. Vu, and R.-Y. Kim, "Implemental control strategy for grid stabilization of grid-connected PV system based on German grid code in symmetrical low-to-medium voltage network," *IEEE Trans. Energy Convers.*, vol. 28, no. 3, pp. 619–631, Sep. 2013.

[16] B. Wen, D. Boroyevich, R. Burgos, P. Mattavelli, and Z. Shen, "Analysis of D-Q small-signal impedance of grid-tied inverters," *IEEE Trans. Power Electron.*, vol. 31, no. 1, pp. 675–687, Jan. 2016.

[17] D. Dong, B. Wen, D. Boroyevich, P. Mattavelli, and Y. Xue, "Analysis of phase-locked loop low-frequency stability in three-phase grid-connected power converters considering impedance interactions," *IEEE Trans. Ind. Electron.*, vol. 62, no. 1, pp. 310–321, Jan. 2015.

[18] N. Guruwacharya, "Probing signal-based data-driven modeling of power electronics smart converter dynamics using power hardware-in-the-loop," Ph.D. dissertation, Dept. Elect. Eng. Comput. Sci., South Dakota State Univ., Brookings, South Dakota, 2023.

[19] J. Matevosyan, B. Badrzadeh, T. Prevost, E. Quitmann, D. Ramasubramanian, H. Urdal, S. Achilles, J. MacDowell, S. H. Huang, V. Vital, J. O'Sullivan, and R. Quint, "Grid-forming inverters: Are they the key for high renewable penetration?" *IEEE Power Energy Mag.*, vol. 17, no. 6, pp. 89–98, Nov. 2019.

[20] S. Subedi, B. Poudel, P. Aslami, R. Fourney, H. M. Rekabdarkolaee, R. Tonkoski, and T. M. Hansen, "Automated data-driven model extraction and validation of inverter dynamics with grid support function," *e-Prime Adv. Electr. Eng., Electron. Energy*, vol. 6, Dec. 2023, Art. no. 100365.

[21] G. Guarderas, A. Frances, D. Ramirez, R. Asensi, and J. Uceda, "Blackbox large-signal modeling of grid-connected DC–AC electronic power converters," *Energies*, vol. 12, no. 6, p. 989, Mar. 2019.

[22] *IEEE Standard for Interconnection and Interoperability of Distributed Energy Resources With Associated Electric Power Systems Interfaces*, IEEE Standard 1547-2018, Revision of IEEE Standard 1547-2003, Apr. 2018.

[23] N. Guruwacharya, N. Bhujel, T. M. Hansen, S. Suryanarayanan, R. Tonkoski, U. Tamrakar, and F. Wilches-Bernal, "Modeling inverters with grid support functions for power system dynamics studies," in *Proc. IEEE Power Energy Soc. Innov. Smart Grid Technol. Conf. (ISGT)*, Feb. 2021, pp. 1–5.

[24] H. D. Abbood and A. Benigni, "Data-driven modeling of a commercial photovoltaic microinverter," *Model. Simul. Eng.*, vol. 2018, pp. 1–11, Apr. 2018.

[25] V. Valdivia, A. Lazaro, A. Barrado, P. Zumel, C. Fernandez, and M. Sanz, "Black-box modeling of three phase voltage source inverters based on transient response analysis," in *Proc. 25th Annu. IEEE Appl. Power Electron. Conf. Expo. (APEC)*, Feb. 2010, pp. 1279–1286.

[26] N. Guruwacharya, N. Bhujel, U. Tamrakar, M. Rauniyar, S. Subedi, S. E. Berg, T. M. Hansen, and R. Tonkoski, "Data-driven power electronic converter modeling for low inertia power system dynamic studies," in *Proc. IEEE Power Energy Soc. Gen. Meeting (PESGM)*, Aug. 2020, pp. 1–5.

[27] N. Guruwacharya, H. Bhandari, S. Subedi, J. D. Vasquez-Plaza, M. L. Stoel, U. Tamrakar, F. Wilches-Bernal, F. Andrade, T. M. Hansen, and R. Tonkoski, "Data-driven modeling of commercial photovoltaic inverter dynamics using power hardware-in-the-loop," in *Proc. Int. Symp. Power Electron., Electr. Drives, Autom. Motion (SPEEDAM)*, Jun. 2022, pp. 924–929.

[28] N. A. Ninad, D. Turcotte, and T. H. M. El-Fouly, "Grid-interactive inverter modeling for power system studies," in *Proc. IEEE Power Energy Soc. Gen. Meeting*, Jul. 2015, pp. 1–5.

[29] R. D. Middlebrook and S. Cuk, "A general unified approach to modelling switching-converter power stages," in *Proc. IEEE Power Electron. Specialists Conf.*, Jun. 1976, pp. 18–34.

[30] S. Subedi, M. Rauniyar, S. Ishaq, T. M. Hansen, R. Tonkoski, M. Shirazi, R. Wies, and P. Cicilio, "Review of methods to accelerate electromagnetic transient simulation of power systems," *IEEE Access*, vol. 9, pp. 89714–89731, 2021.

[31] N. Kroutikova, C. A. Hernandez-Aramburo, and T. C. Green, "State-space model of grid-connected inverters under current control mode," *IET Electr. Power Appl.*, vol. 1, no. 3, pp. 329–338, 2007.

[32] V. Valdivia, A. Lazaro, A. Barrado, P. Zumel, C. Fernandez, and M. Sanz, "Black-box modeling of three-phase voltage source inverters for system-level analysis," *IEEE Trans. Ind. Electron.*, vol. 59, no. 9, pp. 3648–3662, Sep. 2012.

[33] F. A. Alskran, "Dynamic modeling and analysis of the three-phase voltage source inverter under stand-alone and grid-tied modes," M.S. thesis, Dept. Elect. Comput. Eng., Kansas State Univ., Manhattan, Kansas, 2014.

[34] J.-Y. Choi, B. H. Cho, H. F. VanLandingham, H.-S. Mok, and J.-H. Song, "System identification of power converters based on a black-box approach," *IEEE Trans. Circuits Syst. I, Fundam. Theory Appl.*, vol. 45, no. 11, pp. 1148–1158, Nov. 1998.

[35] L. Ljung, *System Identification: Theory for the User*, 2nd ed. Upper Saddle River, NJ, USA: Prentice-Hall, 1999.

[36] *System Identification Toolbox*. Accessed: Apr. 9, 2024. [Online]. Available: https://www.mathworks.com/help/ident/index.html?s_tid=CRUX_lftnav

[37] F. Alonge, F. D'Ippolito, F. M. Raimondi, and S. Tumminaro, "Nonlinear modeling of DC/DC converters using the Hammerstein's approach," *IEEE Trans. Power Electron.*, vol. 22, no. 4, pp. 1210–1221, Jul. 2007.

[38] A. Francés, R. Asensi, O. García, R. Prieto, and J. Uceda, "Modeling electronic power converters in smart DC microgrids—An overview," *IEEE Trans. Smart Grid*, vol. 9, no. 6, pp. 6274–6287, Nov. 2018.

[39] L. Arnedo, D. Boroyevich, R. Burgos, and F. Wang, "Polytopic black-box modeling of DC–DC converters," in *Proc. IEEE Power Electron. Specialists Conf.*, Jun. 2008, pp. 1015–1021.

[40] A. Yazdani and R. Iravani, *Voltage-Sourced Converters in Power Systems: Modeling, Control, and Applications*. Hoboken, NJ, USA: Wiley, 2010.

[41] M. Rasheduzzaman, J. A. Mueller, and J. W. Kimball, "An accurate small-signal model of inverter- dominated islanded microgrids using *dq* reference frame," *IEEE J. Emerg. Sel. Topics Power Electron.*, vol. 2, no. 4, pp. 1070–1080, Dec. 2014.

[42] O. Nelles, *Nonlinear System Identification: From Classical Approaches to Neural Networks, Fuzzy Models and Gaussian Processes*. Springer, 2021.

[43] A. H. Tan and K. R. Godfrey, *Industrial Process Identification Perturbation Signal Design and Applications*. Cham, Switzerland: Springer, 2019.

[44] M. Rauniyar, S. Berg, S. Subedi, T. M. Hansen, R. Fourney, R. Tonkoski, and U. Tamrakar, "Evaluation of probing signals for implementing moving horizon inertia estimation in microgrids," in *Proc. 52nd North Amer. Power Symp. (NAPS)*, Apr. 2021, pp. 1–6.

[45] *Time Domain Specifications*. Accessed: Apr. 9, 2024. [Online]. Available: https://www.tutorialspoint.com/control_systems/control_systems_time_domain_specifications.htm

[46] A. Novak, L. Simon, F. Kadlec, and P. Lotton, "Nonlinear system identification using exponential swept-sine signal," *IEEE Trans. Instrum. Meas.*, vol. 59, no. 8, pp. 2220–2229, Aug. 2010.

[47] R. Chakraborty, H. Jain, and G.-S. Seo, "A review of active probing-based system identification techniques with applications in power systems," *Int. J. Electr. Power Energy Syst.*, vol. 140, Sep. 2022, Art. no. 108008. [Online]. Available: https://www.sciencedirect.com/science/article/pii/S0142061522000539

[48] S. Subedi, N. Guruwacharya, R. Fourney, H. M. Rekabdarkolaee, R. Tonkoski, T. M. Hansen, U. Tamrakar, and P. Cicilio, "Computationally efficient partitioned modeling of inverter dynamics with grid support functions," in *Proc. 47th Annu. Conf. IEEE Ind. Electron. Soc. (IECON)*, Oct. 2021, pp. 1–6.

[49] *Dynapower Powering a Cleaner Planet*. Accessed: Apr. 9, 2024. [Online]. Available: https://dynapower.com/products/energy-storage/mps-125-energy-storage-inverter/

[50] S. Chakraborty, J. Park, G. Saraswat, T. Meyers, J. Wang, S. Tiwari, A. Maqsood, A. Somani, and M. V. Salapaka, "Novel power-hardware-in-the-loop interface method for grid-forming inverter systems," in *Proc. 48th Annu. Conf. IEEE Ind. Electron. Soc. (IECON)*, Oct. 2022, pp. 1–6.

NISCHAL GURUWACHARYA (Student Member, IEEE) received the B.E. degree in electrical engineering and the M.Sc. degree in energy systems planning and management from Tribhuvan University, Nepal, in 2013 and 2019, respectively. He is currently pursuing the Ph.D. degree in electrical engineering with South Dakota State University, Brookings, SD, USA. His research interests include the data-driven modeling of power electronics converters, power electronics and control, and the grid integration of renewable energy systems.

SOHAM CHAKRABORTY (Member, IEEE) received the B.E. degree in electrical engineering from Bengal Engineering and Science University, Shibpur, India, in 2013, and the M.Tech. degree in electrical engineering from Indian Institute of Technology Bombay, Mumbai, in 2016. He is currently pursuing the Ph.D. degree in electrical engineering with the University of Minnesota. He was associated with Indian Institute of Science, Bengaluru, as a Junior Research Fellow on a project funded by the Department of Science and Technology, India.

GOVIND SARASWAT (Senior Member, IEEE) received the Bachelor of Technology degree in electrical engineering from Indian Institute of Technology Delhi, New Delhi, India, in 2007, and the Ph.D. degree from the University of Minnesota Twin Cities, Minneapolis, MN, USA, in 2014, with a focus on control system and dynamics. He is currently a Systems Engineer with Enphase Energy. He was a Researcher with the National Renewable Energy Laboratory, where his research interests include power system modeling and analysis, measurement-based operation and control, machine learning, and optimization.

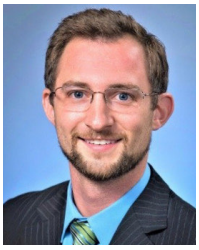

RICHARD BRYCE (Senior Member, IEEE) received the bachelor's and master's degrees in physics from Central Michigan University, Michigan, MI, USA, in 2013 and 2015, respectively, and the Ph.D. degree from the University of Massachusetts Amherst, Amherst, MA, USA, in 2020, with focus on predictive and dynamic techniques for mitigating the variability of photovoltaic power generation within a campus microgrid. He is currently a Researcher with the National Renewable Energy Laboratory, where his research interests include machine learning, power system modeling and analysis, and optimization.

TIMOTHY M. HANSEN (Senior Member, IEEE) received the B.S. degree in computer engineering degree from Milwaukee School of Engineering, Milwaukee, WI, USA, in 2011, and the Ph.D. degree in electrical engineering degree from Colorado State University, Fort Collins, CO, USA, in 2015.

He is currently the Harold C. Hohbach Endowed Associate Professor with the Electrical Engineering and Computer Science Department, South Dakota State University, Brookings, SD, USA. His research interests include the areas of optimization, high-performance computing, and electricity market applications to sustainable power and energy systems, converter-dominated power systems, and cyber-physical-social systems.

REINALDO TONKOSKI (Senior Member, IEEE) received the B.A.Sc. degree in control and automation engineering and the M.Sc. degree in electrical engineering from Pontifícia Universidade Católica do RS (PUC-RS), Brazil, in 2004 and 2006, respectively, and the Ph.D. degree from Concordia University, Canada, in 2011.

Currently, he is a Professor and the Chair for Electric Power Transmission and Distribution with the Technical University of Munich. He has authored over 100 technical publications in peer reviewed journals and conferences. He is also an Editor of IEEE TRANSACTIONS ON SUSTAINABLE ENERGY, IEEE ACCESS, and IEEE SYSTEMS JOURNAL. His research interests include the grid integration of sustainable energy technologies, energy management, power electronics, and control systems.